Extremely Light Carriers in a Two-Dimensional Fermi Surface of 1,3-DAP Molecule Intercalated WSe_2

Xinyue Li(李心悦)[1,2], Jun Deng(邓俊)[3], Boqin Song(宋伯钦)[1], Jing Chen(陈婧)[1], Yuan Lin(林源)[1,2], Qi Li(李琦)[1,2], Qinghua Zhang(张庆华)[1], and Jian-gang Guo(郭建刚)[1*]

[1]*Beijing National Laboratory for Condensed Matter Physics, Institute of Physics, Chinese Academy of Sciences, Beijing 100190, China*
[2]*School of Physical Sciences, University of Chinese Academy of Sciences, Beijing 100049, China*
[3]*Center for High Pressure Science and Technology Advanced Research, Beijing 100193, China*

(Received 12 December 2025; accepted manuscript online 20 January 2026)

Band inversion induced by spin–orbit coupling in topological semimetals typically generates light charge carriers with high Fermi velocities, which are highly desirable for low-dissipation and coherent quantum transport in topological devices. The presence of these carriers in real materials strongly depends on the Fermi-level position. 2M-WSe_2, with its topological and van der Waals nature, serves as an ideal platform for studying quantum transport in two-dimensional systems, despite the fact that interlayer coupling suppresses the formation of light carriers. In this study, we solvothermally intercalate 1,3-diaminopropane molecules into the interlayer space of 2M-WSe_2; these molecules effectively adapt to the electronic structure by eliminating interlayer coupling. Simultaneously, slight electron doping via charge transfer results in a small Fermi pocket with an extremely light effective mass, 0.04–0.06 m_e, as revealed by quantum oscillation measurements. This study demonstrates that molecular intercalation is an effective approach for engineering van der Waals topological materials to achieve specific quantum transport properties.

DOI: 10.1088/0256-307X/43/3/030709 CSTR: 32039.14.0256-307X.43.3.030709

2M-WSe_2 has been identified as a weak topological semimetal comprising a stack of quantum spin Hall layers protected by time-reversal symmetry.[1–3] The band inversion between W-5d and Se-4p orbitals yields nontrivial electronic states characterized by high Fermi velocities and small band curvature, which collectively produce light carriers with high mobility. Such light quasiparticles are highly desirable for realizing low-dissipation and coherent charge transport, offering opportunities for studying quantum transport phenomena and developing high-speed or low-power electronic functionalities. However, previous studies have revealed that interlayer coupling in 2M-WSe_2 significantly modifies the expected two-dimensional electronic structure,[4] thereby suppressing the emergence of these light carriers.

Chemical intercalation, which is the process of inserting guest species, such as atoms, ions, or molecules, into the van der Waals gaps of layered host materials, serves as a versatile and powerful approach to material engineering.[5] This approach enables direct modulation with high precision, renders the materials compatible with diverse intercalants, and has low energy and temperature requirements. By leveraging charge transfer and van der Waals gap expansion to achieve specific interlayer interactions, intercalation can induce phase transitions,[6–8] drive superconducting states,[9–13] reduce thermal conductivity,[14–16] enhance structural flexibility,[17] and facilitate exfoliation.[18–20] Given the pronounced sensitivity of 2M-WSe_2 to interlayer coupling, intercalation offers an effective route for tuning its electronic properties and Fermi surface dimensionality.[3] Nonetheless, the introduction of structural disorder and scattering centers by inserted molecules, along with potential framework defects generated by soft-chemistry routes such as solvothermal intercalation, remains a major challenge. Consequently, achieving high-mobility quantum transport in layered materials via intercalation remains a challenge.

In this study, we employed a solvothermal intercalation strategy using 1,3-diaminopropane (1,3-DAP) to engineer the lattice and electronic structure of 2M-WSe_2. Remarkably, we observed Shubnikov–de Haas (SdH) oscillations in intercalated $(1,3\text{-DAP})_{0.3}WSe_2$ with an onset field below 3 T, which persisted up to 30 K despite a reduction in both the residual resistivity ratio (RRR) and transport mobility. These anomalous oscillations revealed multiple Fermi pockets with extremely light effective masses and high quantum mobilities. To clarify the origin of these light carriers, we demonstrate that the expansion of the van der Waals gap eliminates the interlayer coupling, leading to a typical two-dimensional electronic structure. Furthermore, our calculations indicate that 1,3-DAP intercalation not only increases the interlayer spacing but also induces slight in-plane lattice compression, populating

*Corresponding author. Email: jgguo@iphy.ac.cn
© 2026 Chinese Physical Society and IOP Publishing Ltd. All rights, including for text and data mining, AI training, and similar technologies, are reserved.

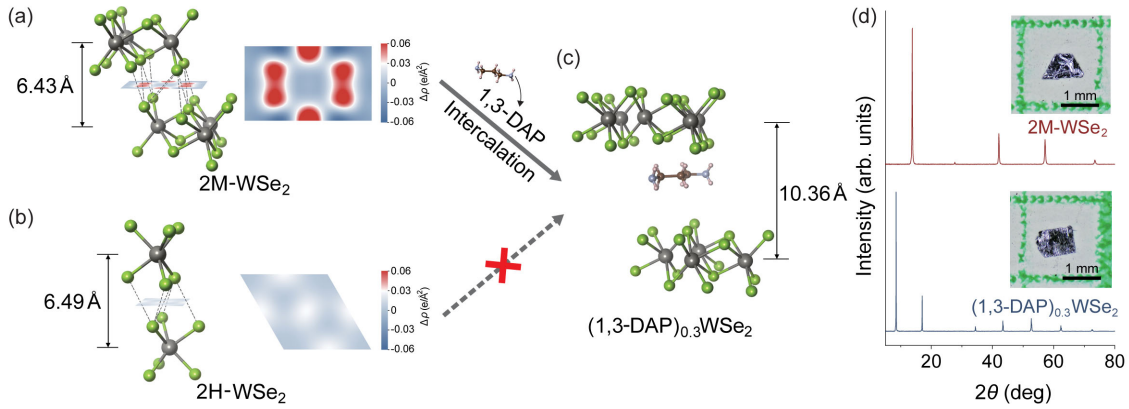

Fig. 1. Structural evolution of WSe_2 upon 1,3-DAP intercalation. (a) Crystal structure and interlayer charge density difference of 2M-WSe_2, with an interlayer spacing of 6.43 Å. (b) Crystal structure and interlayer charge density difference of 2H-WSe_2, with an interlayer spacing of 6.49 Å. (c) Crystal structure of $(1,3\text{-DAP})_{0.3}WSe_2$, showing expanded interlayer spacing of 10.36 Å after 1,3-DAP intercalation. (d) X-ray diffraction (XRD) patterns of the $(00l)$ plane for single-crystal 2M-WSe_2 and $(1,3\text{-DAP})_{0.3}WSe_2$, with insets showing the corresponding optical images.

a small electron pocket responsible for the observed light carriers. These results establish that molecular intercalation is a viable and effective strategy for engineering extremely light carriers and low-dimensional Fermi surfaces, thereby enabling pronounced quantum transport phenomena in layered topological materials.

Figure 1(a) illustrates the structural evolution of WSe_2 during the 1,3-DAP intercalation. 2M-WSe_2 exhibits a layered structure with a 6.43 Å interlayer distance, and the cross-sectional plot of the charge density difference between layers in the 2M phase reveals strong interlayer coupling. In contrast, the 2H phase [Fig. 1(b)] shows considerably weaker interlayer coupling, with a slightly larger interlayer distance of 6.49 Å. Subsequently, 1,3-DAP was intercalated into the 2M phase, resulting in an increase in interlayer spacing to 10.34 Å [Fig. 1(c)]. Notably, successful intercalation of 1,3-DAP was observed only in 2M-WSe_2. Through the intercalation process, the significant structural changes observed in 2M-WSe_2 and $(1,3\text{-DAP})_{0.3}WSe_2$ were confirmed by $(00l)$-plane X-ray diffraction (XRD) patterns [see Fig. 1(d)] and scanning transmission electron microscopy (STEM; see Fig. S2 in the Supplementary Materials) of single crystals.

The intercalation behavior of 1,3-DAP in WSe_2 is closely related to the charge transfer between the intercalant and the host material. In the 2H phase, the weak interlayer differential charge density suggests a limited charge transfer. Similarly, as a neutral molecule, the charge transfer of 1,3-DAP is weak. Consequently, 1,3-DAP cannot be successfully inserted into the 2H phase, which is consistent with the negative intercalation results in our experiments. In contrast, ions, including organic cations such as THA^+ [21] and CTA^+, [22] and alkali metal ions such as Li^+ [23] and K^+, [24] can be intercalated into 2H-WSe_2 via electrochemical or hydrothermal methods, as their charge enhances interactions with the host layers, promoting charge transfer and stabilizing the intercalated state. Additionally, some neutral molecules with polar functional groups, [25] even those without a net charge, can interact with 2H-WSe_2 through hydrogen bonding or dipole interactions, inducing charge redistribution and enabling successful intercalation via a solvothermal method. The successful intercalation of 2H-WSe_2 is primarily governed by charge transfer, either through the insertion of charged species or neutral molecules with polar functional groups that facilitate charge redistribution via hydrogen bonding or dipole interactions.

In the 2M phase, the significantly enhanced interlayer charge density difference indicates stronger interlayer coupling and possible formation of "quasi-covalent" bonding [26–28] between Se atoms across two adjacent layers, shown as pronounced charge accumulation of the charge density difference at the connection points between interlayer Se-Se atoms [inset of 2M-WSe_2 in Fig. 1(a)]. This might promote charge transfer between 1,3-DAP and the 2M-WSe_2 lattice, stabilizing the intercalation, which explains the successful intercalation of 1,3-DAP into 2M-WSe_2 under hydrothermal conditions, in contrast to that into the 2H-phase. The introduction of 1,3-DAP increases the interlayer spacing and weakens the interlayer interaction, which is expected to have an important influence on the electronic structure.

To quantify these changes, we measured the electrical transport properties of 2M-WSe_2 and $(1,3\text{-DAP})_{0.3}WSe_2$ in single-crystal samples. Figure 2(a) shows the temperature-dependent resistivity $\rho(T)$ of 2M-WSe_2. Below 50 K, the resistivity exhibits a temperature dependence that approaches quadratic behavior, suggesting Fermi liquid behavior. Moreover, 2M-WSe_2 exhibits an RRR of approximately 30, which is indicative of reasonably good crystalline quality with relatively low disorder. Figure 2(b) shows the temperature dependence of the resistivity of $(1,3\text{-DAP})_{0.3}WSe_2$. However, after intercalation, the RRR decreases to 4.1, indicating the presence of additional scattering centers introduced by lattice distortion and that of intercalated molecules within the van der Waals gaps. Additionally, an increase in resistivity was observed as the temperature decreased below 6.6 K. In our previous studies, the intercalation of 1,3-DAP into $SnSe_2$ resulted in an anomalous increase in resistance, leading to an extremely

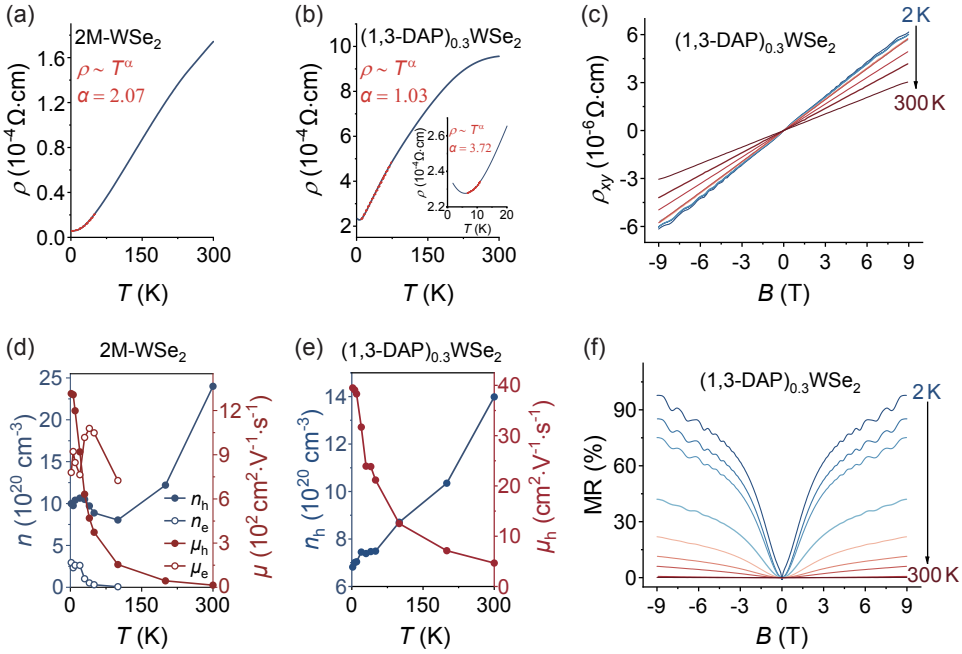

Fig. 2. Electrical transport properties of 2M-WSe_2 and $(1,3\text{-DAP})_{0.3}WSe_2$. (a) Temperature dependence of the resistivity, $\rho(T)$, for 2M-WSe_2. (b) Temperature dependence of the resistivity, $\rho(T)$, for $(1,3\text{-DAP})_{0.3}WSe_2$. (c) Magnetic field dependence of the Hall resistivity, ρ_{xy}, for $(1,3\text{-DAP})_{0.3}WSe_2$ measured at temperatures ranging from 2 to 300 K. (d) Temperature dependence of the carrier concentration (n) and carrier mobility (μ) for 2M-WSe_2. (e) Temperature dependence of the carrier concentration (n_h) and carrier mobility (μ_h) for $(1,3\text{-DAP})_{0.3}WSe_2$. (f) Magnetic field dependence of the magnetoresistance (MR) at temperatures ranging from 2 to 300 K.

large on-off ratio of 10^7.[29] This phenomenon was attributed to a change in the hydrogen-bonding structure of the amino group from dynamic to static. In contrast to the several orders of magnitude of resistance increase observed in 1,3-DAP intercalated $SnSe_2$, the resistivity of $(1,3\text{-DAP})_{0.3}WSe_2$ changed by only $5 \times 10^{-6}\,\Omega\cdot$cm within 5 K. This indicates that the resistance transition mechanisms in the two systems may be distinct, with the behavior in $(1,3\text{-DAP})_{0.3}WSe_2$ being more likely driven by disorder-induced weak localization. In the range from 11 to 75 K [see inset of Fig. 2(b)], the resistivity follows an approximately linear temperature dependence, which is consistent with the high-temperature regime of the Bloch–Grüneisen (BG) model,[30] which describes electron–phonon-scattering-dominated resistivity. In the intermediate range of 6.6–11 K, the extracted exponent (approximately 3.7) suggests a crossover between the low-temperature T^5 and high-temperature T behaviors of the BG model,[31] with possible additional contributions from weak localization and electron–electron interactions. At temperatures above 75 K, the resistivity deviates from linearity and shows a tendency toward saturation, which is often associated with strong phonon scattering approaching the Mott–Ioffe–Regel limit,[32] although the presence of additional scattering channels introduced by intercalation cannot be excluded.

Figure 2(c) illustrates the Hall resistivity ρ_{xy} of $(1,3\text{-DAP})_{0.3}WSe_2$ measured at temperatures from 2 to 300 K. The ρ_{xy} curves exhibit a linear dependence on the magnetic field, with the slope decreasing as the temperature increases. The slope of the ρ_{xy} curves is positive, indicating that the dominant charge carriers in $(1,3\text{-DAP})_{0.3}WSe_2$ are holes. Figure 2(d) shows the fitting of the Hall resistivity of n-p-compensated 2M-WSe_2 (see Fig. S4) using a two-carrier model, which reveals two types of charge carriers. In contrast, figure 2(e) presents the temperature dependence of the hole carrier concentration n_h and mobility μ_h for $(1,3\text{-DAP})_{0.3}WSe_2$, derived from the Hall resistivity in Fig. 2(c) using a single-carrier model. The carrier concentration after intercalation is slightly reduced but remains comparable to that of the parent compound, although holes dominate the carriers, suggesting that intercalation induces effective hole doping. Meanwhile, the hole mobility μ_h decreases by two orders of magnitude from approximately $10^3\,cm^2\cdot V^{-1}\cdot s^{-1}$ before intercalation to approximately $10^1\,cm^2\cdot V^{-1}\cdot s^{-1}$ afterward, which can be attributed to the structural defects induced by the intercalation. These changes significantly reduce the scattering time, leading to a drastic reduction in mobility. Figure 2(f) shows the magnetoresistance (MR) in the range from 2 to 300 K with pronounced SdH oscillations. The MR oscillations can be tracked down to a field as low as $B \approx 3$ T and are sustained up to 30 K. Remarkably, the observation of SdH oscillations at a field as low as 3 T is unexpected with such low mobility and RRR.[33] The mobility estimated from the onset magnetic field is on the order of $\frac{1}{B_{onset}} \approx 3000\,cm^2\cdot V^{-1}\cdot s^{-1}$, which is considerably higher than the Hall mobility.

To further understand the origin of these unusual transport behaviors, detailed quantum oscillation measurements were performed. The oscillatory component ΔR_{xx} was obtained by subtracting the smooth background

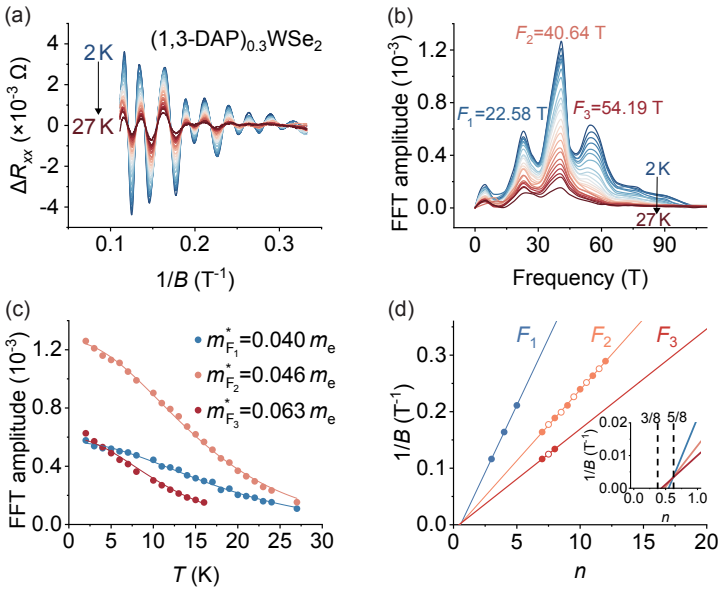

Fig. 3. SdH oscillations in $(1,3\text{-DAP})_{0.3}WSe_2$. (a) Oscillatory component ΔR_{xx} as the function of $1/B$ at various temperatures from 2 to 27 K. Note that ΔR_{xx} is obtained by subtracting a smooth background from R_{xx}. (b) FFT amplitudes of the SdH oscillations. (c) Temperature dependence of FFT amplitudes of F_1, F_2, and F_3 peaks. Solid lines represent fits to the Lifshitz–Kosevich formula used to obtain effective masses. (d) Landau index n plotted against $1/B$ for the frequencies F_1, F_2, and F_3, derived from the ΔR_{xx} curve at 2 K. The closed and open circles indicate the integer index (ΔR_{xx} peak) and half integer index (ΔR_{xx} valley), respectively. Inset: enlarged fitting lines around the intercept.

from R_{xx}. In Fig. 3(a), ΔR_{xx} is plotted as a function of $1/B$ from 2 to 27 K. Complex periodic behaviors of ΔR_{xx} indicate the contributions of more than one frequency component. Three main frequencies, $F_1 = 22.58$ T, $F_2 = 40.64$ T, and $F_3 = 54.19$ T, were identified from the fast Fourier transform (FFT) spectra of SdH oscillations from 3 T to 9 T in Fig. 3(b). Two low-frequency SdH oscillations are still observed at 27 K, whereas the high-frequency oscillations disappear at 15 K. According to the Onsager relation $F = (\Phi_0/2\pi^2)A_F$, the perpendicular cross-sections of the Fermi surface relative to the magnetic field are $A_{F_1} = 0.00215\,\text{Å}^{-2}$, $A_{F_2} = 0.00387\,\text{Å}^{-2}$, and $A_{F_3} = 0.00516\,\text{Å}^{-2}$. The SdH oscillations observed with multiple frequencies can be analyzed through the superposition of individual oscillatory components, each of which can be described by the Lifshitz–Kosevich formula:[34,35]

$$\Delta\rho_{xx} \propto \frac{2\pi^2 k_B T/\hbar\omega_c}{\sinh(2\pi^2 k_B T/\hbar\omega_c)} \cdot e^{-2\pi^2 k_B T_D/\hbar\omega_c} \cos 2\pi\left(\frac{F}{B} + \gamma - \delta\right), \quad (1)$$

where ω_c is the cyclotron frequency, T_D is the Dingle temperature, and F is the frequency; γ is defined as $\gamma = \frac{1}{2} - \frac{\Phi_B}{2\pi}$, and Φ_B is the Berry's phase. The phase shift δ accounts for the dimensionality of the Fermi surface (FS). Specifically, $\delta = 0$ in a two-dimensional Fermi surface, while $\delta = \pm 1/8$ in a three-dimensional system. As shown in Fig. 3(c), the temperature dependence of the FFT peak amplitudes can be fitted using a temperature damping factor $R_T = \frac{2\pi^2 k_B T/\hbar\omega_c}{\sinh(2\pi^2 k_B T/\hbar\omega_c)}$ to extract the following effective masses: $m^*_{F_1} = 0.040\,m_e$, $m^*_{F_2} = 0.046\,m_e$, and $m^*_{F_3} = 0.063\,m_e$. This demonstrates the presence of extremely light carriers in this intercalation system. To the best of our knowledge, we compared the effective masses of $(1,3\text{-DAP})_{0.3}WSe_2$ with those of pristine 2M-WSe_2 and intercalated TMDs. The effective mass observed in our intercalated system is much smaller than that of previously reported TMD-based materials, as listed in Table 1. The oscillation curve was fitted using Eq. (1), from which the parameters of the three frequencies were determined, as shown in Fig. S5 and Table S1. These light carriers from all three pockets exhibit mobilities on the order of $10^3\,\text{cm}^2\cdot\text{V}^{-1}\cdot\text{s}^{-1}$, which is close to the estimated value from the onset magnetic field and significantly higher than the Hall mobility ($\sim 10^1\,\text{cm}^2\cdot\text{V}^{-1}\cdot\text{s}^{-1}$). This suggests that the SdH oscillations are independent of the majority of the hole-type carriers observed in the Hall measurements. This arises from the fact that extremely light pockets are extremely low-density minority carriers despite their high quantum mobility, whose contribution to the Hall response is negligible compared with that of the dominant hole band, thereby preserving the linear Hall response (see Fig. S6). SdH oscillations select a low-density minority carrier pocket with high quantum mobility, whereas the Hall response and transport mobility are dominated by strongly scattered majority carriers. The Landau fan diagram at 2 K is shown in Fig. 3(d). The LL integer index n corresponds to the peaks of ΔR_{xx}, whereas the half-integer index $n+1/2$ is assigned to the valleys of ΔR_{xx}. The intercepts obtained from the linear fits of n as a function of $1/B$ for the three main frequencies are 0.55, 0.49, and 0.43 [inset of Fig. 3(d)]. The corresponding Berry's phases, derived from the fitted intercepts according to $\Phi_B = 2\pi(\frac{1}{2} - \gamma)$, are close to zero, indicating their trivial nature. Their deviations from $\delta = \pm 1/8$ suggest the 2D nature of FSs.

Table 1. Comparison of effective masses in pristine 2M-WSe_2 and related intercalated TMDs.

Materials	Host	Guest	Effective mass (m_e)	Reference
2M-WSe_2	–	–	0.27–0.39	[4]
$InTaS_2$	TaS_2	In	0.2	[36]
$Ba_6Nb_{11}S_{28}$	NbS_2	Ba_3NbS_5	0.33–1.95	[37]
$SrTa_2S_5$	TaS_2	Sr_3TaS_5	0.15–1.02	[38]
$(1,3\text{-DAP})_{0.3}WSe_2$	2M-WSe_2	1,3-DAP	0.04–0.063	This work

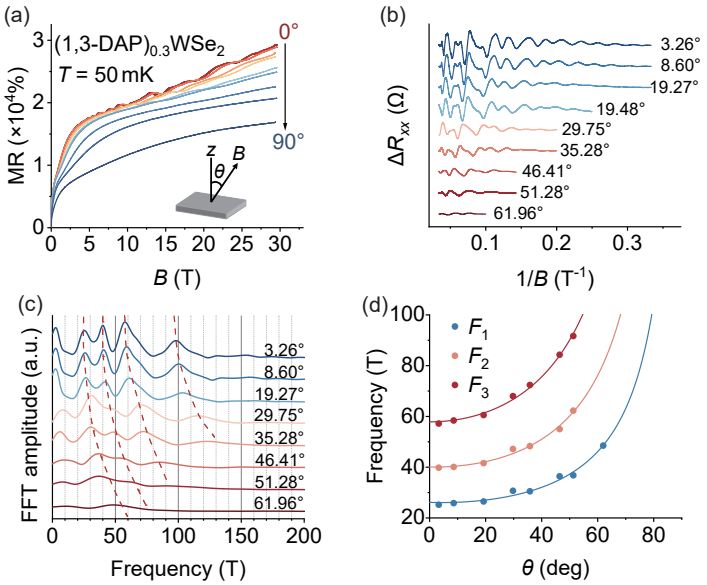

Fig. 4. Angular dependence of oscillations of $(1,3\text{-DAP})_{0.3}WSe_2$. (a) MR at various field directions at $T = 50$ mK. Inset: definition of θ. (b) Oscillatory component ΔR_{xx} as a function of $1/B$ in various field directions. (c) FFT amplitudes of the oscillations in various field directions. (d) Angular dependence of three main oscillation frequencies: F_1, F_2, and F_3. Curves are fitting lines corresponding to the formula $F(\theta) = F(0°)/\cos\theta$.

Further evidence of the 2D Fermi surface characteristics in $(1,3\text{-DAP})_{0.3}WSe_2$ was obtained by analyzing the evolution of the SdH oscillations at different magnetic field angles. Figure 4(a) presents the MR as a function of the magnetic field at different angles θ from 0° (field perpendicular to the sample plane) to 90° (field parallel to the plane) at 50 mK. The experimental configuration is shown in the inset of Fig. 4(a). MR shows a pronounced dependence on the field direction. This angular dependence reflects the anisotropic structure of FSs. Figure 4(b) displays the oscillatory component ΔR_{xx} as a function of $1/B$ at various field directions. Clear oscillations can only be observed at $\theta < 60°$, indicating the 2D nature. As shown in Fig. 4(c), the FFT amplitudes in various field directions exhibit four main frequencies, indicating that a new oscillation frequency emerges at a magnetic field above 9 T. As θ increases, the magnetic field positions corresponding to each frequency shift toward higher fields. Figure 4(d) shows the evolution of the frequencies, denoted by the red dashed lines in Fig. 4(c). Fitting curves of three main frequencies all correspond to a $1/\cos\theta$ function, which describes the angular dependence expected for 2D FSs. The excellent agreement between the experimental data and the fit provides strong evidence that the SdH oscillations arise from 2D FSs.

We performed theoretical calculations based on the structures of 2M-WSe_2 and $(1,3\text{-DAP})_{0.3}WSe_2$ to clarify the electronic origin of the light carriers. For $(1,3\text{-DAP})_{0.3}WSe_2$, a monolayer 2M-$WSe_2$ model with applied in-plane compressive strain was adopted. This model is a reasonable approximation because intercalation significantly weakens interlayer coupling. As shown in Fig. S9, the electronic structure of $(1,3\text{-DAP})_{0.3}WSe_2$, corresponding to $\Delta d = 4$ Å, closely resembles that of a relaxed monolayer, suggesting that the interlayer coupling becomes weak and the material behaves similarly to a single layer. STEM observations show that, in addition to interlayer expansion, the in-plane lattice parameters of the inorganic layers decrease to some extent (see Fig. S11). Geometrical optimization of the intercalated structure supports a similar trend of in-plane lattice contraction, which is consistent with the experimental observations (see Fig. S12 and Table S2). To fit this structural feature, an in-plane compressive strain was introduced into the monolayer model. Such a lattice-compressive behavior may arise from interfacial stress or doping-induced changes in the bonds, both of which can lead to lattice responses. Similar behavior has been reported for other hole-doped materials.[39,40]

As shown in Figs. 5(a) and 5(b), the intercalation of 1,3-DAP leads to a significant modification of the band structure. The intercalated phase exhibits semimetal characteristics (DOS; see Fig. S13), which are consistent with the transport results. Figures 5(c) and 5(d) further illustrate this transition through Fermi surface evolution. In 2M-WSe_2 [Fig. 5(c)], the Fermi surface exhibits a notable interlayer extension, suggesting strong interlayer coupling.

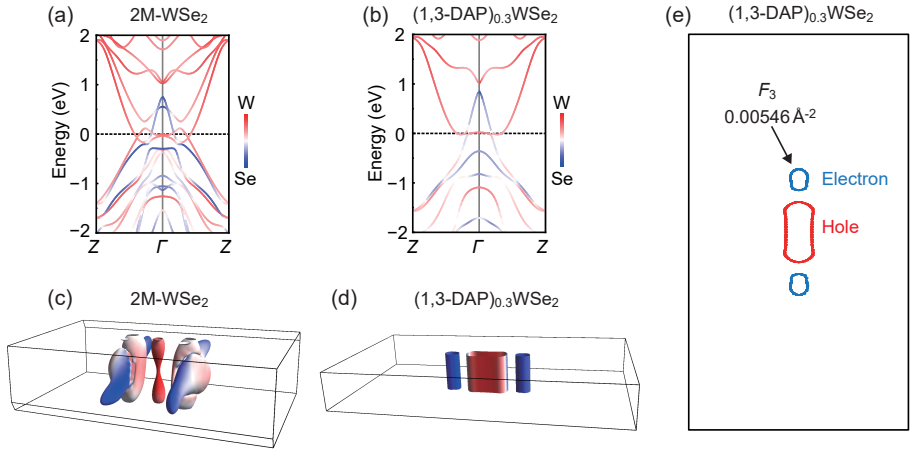

Fig. 5. Electronic structure evolution in 2M-WSe_2 and $(1,3\text{-DAP})_{0.3}WSe_2$. (a) and (b) Calculated band structures of pristine 2M-WSe_2 and intercalated $(1,3\text{-DAP})_{0.3}WSe_2$ along the in-plane Γ–Z direction, which corresponds to the high-dispersion direction within the WSe_2 layers. (c) and (d) FSs of 2M-WSe_2 and $(1,3\text{-DAP})_{0.3}WSe_2$, respectively. (e) Cross-sectional view of the FS of $(1,3\text{-DAP})_{0.3}WSe_2$.

In contrast, after intercalation [Fig. 5(d)], the Fermi surface becomes more confined within individual layers, indicating the suppression of interlayer coupling. This dimensionality change is consistent with angle-dependent quantum oscillation measurements. In Fig. 5(e), the cross-sectional view of the FS of $(1,3\text{-DAP})_{0.3}WSe_2$ reveals an electron pocket with an area of 0.00546 $Å^{-2}$, which closely matches the experimental frequency F_3 in the SdH oscillations. This indicates that the small electron pocket is responsible for the observed SdH oscillation. Despite representing a minority carrier population, these electrons possess extremely small effective masses and high mobility, allowing them to dominate the quantum oscillation signals, even when they contribute less to the total conductivity. Furthermore, our calculations confirm that the nontrivial band topology of the parent 2M phase, characterized by band inversion and protected surface states, is preserved in the intercalated structure (see Supplementary Materials for details). The near-zero Berry's phase experimentally obtained reflects a trivial bulk pocket within a topologically nontrivial system.

In conclusion, we have demonstrated that solvothermal intercalation with 1,3-DAP is an effective strategy for engineering the electronic properties of weak topological semimetal 2M-WSe_2. By successfully expanding the van der Waals gap and eliminating the detrimental interlayer coupling, we restored the ideal two-dimensional electronic structure. Combined with the slight strain induced by the interaction between the host and insertion layers, this process creates a small electron pocket with an extremely light effective mass, as revealed by robust quantum oscillations. This study not only resolves the key challenge of accessing the intrinsic light carriers in 2M-WSe_2 but also establishes molecular intercalation as a powerful and versatile tool for achieving specific quantum transport phenomena in van der Waals topological materials.

Acknowledgements. This work was supported by the National Key Research and Development Program of China (Grant No. 2023YFA1406301) and the National Natural Science Foundation of China (Grant Nos. 52250308 and 52525205). A part of this study was conducted at the Synergetic Extreme Condition User Facility (SECUF). Some of the numerical computations were performed at the Hefei Advanced Computing Center.

References

[1] Chen P, Pai W W, Chan Y H, Sun W L, Xu C Z, Lin D S, Chou M Y, Fedorov A V, and Chiang T C 2018 *Nat. Commun.* **9** 2003
[2] Ugeda M M, Pulkin A, Tang S, Ryu H, Wu Q, Zhang Y, Wong D, Pedramrazi Z, Martín-Recio A, Chen Y, Wang F, Shen Z X, Mo S K, Yazyev O V, and Crommie M F 2018 *Nat. Commun.* **9** 3401
[3] Xu L, Li Y, Fang Y, Zheng H, Shi W, Chen C, Pei D, Lu D, Hashimoto M, Wang M, Yang L, Feng X, Zhang H, Huang F, Xue Q, He K, Liu Z, and Chen Y 2023 *Adv. Mater.* **35** 2300227
[4] He Y, Strasser A, Hagopian N, Bierman B, Ma H, Fox C, Li Z, Pederson N, Taniguchi T, Watanabe K, Xiao J, Wang Y, Voyles P M, Qian X, and Rhodes D A 2025 *Adv. Funct. Mater.* **35** 2420356
[5] Zhu M T, Wang L, Gao L, Liu J, Lyu X Y, Wang Y Q, Lu C, Li M C, Liu P Y, Song J Y, Tao H Y, Zhao B B, Ji A L, Cao Z X, and Lu N P 2025 *Chin. Phys. Lett.* **42** 037201
[6] Cheng Y, Zhu Y, Han Y, Liu Z, Yang B, Nie A, Huang W, Shahbazian-Yassar R, and Mashayek F 2017 *Chem. Mater.* **29** 1350
[7] Zhu X, Li D, Liang X, and Lu W D 2019 *Nat. Mater.* **18** 141
[8] Yang R, Li Z, and Fan Y 2024 *Nat. Rev. Chem.* **8** 650
[9] Hannay N B, Geballe T H, Matthias B T, Andres K, Schmidt P, and MacNair D 1965 *Phys. Rev. Lett.* **14** 225
[10] Guo J, Jin S, Wang G, Wang S, Zhu K, Zhou T, He M, and Chen X 2010 *Phys. Rev. B* **82** 180520
[11] Kriener M, Segawa K, Ren Z, Sasaki S, Wada S, Kuwabata S, and Ando Y 2011 *Phys. Rev. B* **84** 054513
[12] Ying T P, Chen X L, Wang G, Jin S F, Zhou T T, Lai X F, Zhang H, and Wang W Y 2012 *Sci. Rep.* **2** 426
[13] Ying T, Chen X, Wang G, Jin S, Lai X, Zhou T, Zhang H, Shen S, and Wang W 2013 *J. Am. Chem. Soc.* **135** 2951

[14] Wan C, Wang Y, Wang N, Norimatsu W, Kusunoki M, and Koumoto K 2011 *J. Electron. Mater.* **40** 1271

[15] Zhu G, Liu J, Zheng Q, Zhang R, Li D, Banerjee D, and Cahill D G 2016 *Nat. Commun.* **7** 13211

[16] Sun R, Deng J, Wu X, Hao M, Ma K, Ma Y, Zhao C, Meng D, Ji X, Ding Y, Pang Y, Qian X, Yang R, Li G, Li Z, Dai L, Ying T, Zhao H, Du S, Li G, Jin S, and Chen X 2023 *Nat. Commun.* **14** 6689

[17] Wan C, Gu X, Dang F, Itoh T, Wang Y, Sasaki H, Kondo M, Koga K, Yabuki K, Snyder G J, Yang R, and Koumoto K 2015 *Nat. Mater.* **14** 622

[18] Zeng Z, Sun T, Zhu J, Huang X, Yin Z, Lu G, Fan Z, Yan Q, Hng H H, and Zhang H 2012 *Angew. Chem. Int. Ed.* **51** 9052

[19] Lin Z, Liu Y, Halim U, Ding M, Liu Y, Wang Y, Jia C, Chen P, Duan X, Wang C, Song F, Li M, Wan C, Huang Y, and Duan X 2018 *Nature* **562** 254

[20] Yang R, Mei L, Zhang Q, Fan Y, Shin H S, Voiry D, and Zeng Z 2022 *Nat. Protoc.* **17** 358

[21] Liang J, Li Y, Yin S, and Wan C 2023 *Mater. Today Energy* **36** 101355

[22] He Q, Lin Z, Ding M, Yin A, Halim U, Wang C, Liu Y, Cheng H C, Huang Y, and Duan X 2019 *Nano Lett.* **19** 6819

[23] Shin Y S, Lee K, Duong D L, Kim J S, Kang W T, Kim J E, Won U Y, Lee I, Lee H, Heo J, Lee Y H, and Yu W J 2020 *Adv. Funct. Mater.* **30** 2003688

[24] Ahmad M, Müller E, Habenicht C, Schuster R, Knupfer M, and Büchner B 2017 *J. Phys.-Condens. Mat.* **29** 165502

[25] Zhang C, Fei B, Yang D, Zhan H, Wang J, Diao J, Li J, Henkelman G, Cai D, Biendicho J J, Morante J R, and Cabot A 2022 *Adv. Funct. Mater.* **32** 2201322

[26] Zhao Y, Qiao J, Yu P, Hu Z, Lin Z, Lau S P, Liu Z, Ji W, and Chai Y 2016 *Adv. Mater.* **28** 2399

[27] Kasai H, Tolborg K, Sist M, Zhang J, Hathwar V R, Filsø M Ø, Cenedese S, Sugimoto K, Overgaard J, Nishibori E, and Iversen B B 2018 *Nat. Mater.* **17** 249

[28] Chen Y T, Gong P L, Ren Y T, Hu L, Zhang H, Wang J L, Huang L, and Shi X Q 2021 *J. Phys. Chem. Lett.* **12** 11998

[29] Xie Z, Luo R, Ying T, Gao Y, Song B, Yu T, Chen X, Hao M, Chai C, Yan J, Huang Z, Chen Z, Du L, Zhu C, Guo J, and Chen X 2024 *Nat. Chem.* **16** 1803

[30] Grüneisen E 1933 *Ann. Phys.-Berlin* **408** 530

[31] Liu H, Yu T, Zhang Z, and Ying T 2024 *Chin. Phys. Lett.* **41** 077401

[32] Ioffe A F and Regel A R 1960 *Prog. Semicond.* **4** 237

[33] Zhi Z, Ruan H, Liu J, Li X, Zhang Y, Yao Q, Tang C, Xiao Y, and Kou X 2025 *Chin. Phys. Lett.* **42** 090708

[34] Shoenberg D 1984 *Magnetic oscillations in metals* (Cambridge: Cambridge University Press)

[35] Murakawa H, Bahramy M S, Tokunaga M, Kohama Y, Bell C, Kaneko Y, Nagaosa N, Hwang H Y, and Tokura Y 2013 *Science* **342** 1490

[36] Zhang Y, Gao Y, Pulkkinen A, Guo X, Huang J, Guo Y, Yue Z, Oh J S, Moon A, Oudah M, Gao X J, Marmodoro A, Fedorov A, Mo S K, Hashimoto M, Lu D, Rajapitamahuni A, Vescovo E, Kono J, Hallas A M, Birgeneau R J, Balicas L, Minár J, Hosur P, Law K T, Morosan E, and Yi M 2025 *Nat. Commun.* **16** 4984

[37] Devarakonda A, Inoue H, Fang S, Ozsoy-Keskinbora C, Suzuki T, Kriener M, Fu L, Kaxiras E, Bell D C, and Checkelsky J G 2020 *Science* **370** 231

[38] Devarakonda A, Chen A, Fang S, Graf D, Kriener M, Akey A J, Bell D C, Suzuki T, and Checkelsky J G 2024 *Nature* **631** 526

[39] Avci S, Chmaissem O, Chung D Y, Rosenkranz S, Goremychkin E A, Castellan J P, Todorov I S, Schlueter J A, Claus H, Daoud-Aladine A, Khalyavin D D, Kanatzidis M G, and Osborn R 2012 *Phys. Rev. B* **85** 184507

[40] Noda H, Sakaguchi S, Fujita R, Minami S, Hirakata H, and Shimada T 2023 *Sci. Rep.* **13** 16546